



# Moho depth (crustal thickness) variations under the northeastern midcontinent of North America, based on H-k-c receiver-function analysis

Hongyu Xiao <sup>a</sup> , Stephen Marshak <sup>a</sup>, Michael DeLucia <sup>b</sup> , Xiaodong Song <sup>a,c,\*</sup>

<sup>a</sup> Department of Earth Science and Environmental Change, University of Illinois Urbana-Champaign, IL, USA

<sup>b</sup> Department of Geology and Environmental Geosciences, College of Charleston, Charleston, SC, USA

<sup>c</sup> State Key Laboratory of Deep Earth and Mineral Exploration, School of Earth and Space Sciences, Peking University, Beijing, China



## ARTICLE INFO

Edited by: Dr C Carolina Lithgow-Bertelloni

### Keywords:

Northeastern midcontinent  
Moho  
Craton  
Crust  
Receiver function

## ABSTRACT

Previous studies of crustal thickness variation in the cratonic platform and bordering foreland basin of the USA Midcontinent emphasize that Moho relief exceeds topographic relief by an order of magnitude and exceeds structural relief of the Great Unconformity (the Phanerozoic-Precambrian contact) by a factor of 2 to 3. Consequently, the Moho displays significant local slopes. Unfortunately, traditional receiver-function analysis of depth to the Moho can lead to inaccurate results when applied to steeply sloping Moho. Therefore, to decrease measurement uncertainty due to slopes, we applied the recently developed H-k-c receiver-function method (Li et al., 2018) to the northern and part of the eastern Midcontinent of the United States to produce a higher-resolution map of Moho-depth (i.e., crustal thickness) variation. Results for the central Midcontinent (including the Ozark Plateau and southern Illinois Basin) were reported in Xiao et al. (2022). Here, we extend our coverage eastward and northward, across the Michigan Basin, Grenville front, and western Appalachian Basin.

Our results emphasize that crustal thickness varies by almost 13 km in a region of North America where land-surface varies by less than 0.5 km and where relief of the Great Unconformity varies by a maximum of 7.5 km. In contrast to contemporary orogenic belts, crustal thickness does not correlate directly with either land-surface elevation or with sedimentary cover thickness (i.e., depth to the Great Unconformity). For example, the thickest crust of the study area occurs in the southwestern Illinois Basin, where land surface elevation is about 150 m, and the thinnest crust occurs in north central Indiana, where land-surface elevation is 250 m. There is a rough correspondence between crustal thickness and epeirogenic structures. In general, thinner crust underlies domes and arches, whereas thicker crust underlies basins, but there are exceptions. For example, while crust is relatively thin beneath the Kankakee and Cincinnati Arches, it is relatively thick beneath the Findlay Arch and the Wisconsin Arch, crust beneath the Michigan basin, overall, is thinner than that of the Illinois or Appalachian basins, and crust beneath the Canadian Shield is thinner than that beneath the cratonic platform. Notably, the Moho beneath the Canadian Shield and beneath the cratonic platform west of the Grenville front, displays roughly periodic long-wavelength north-south trending undulations. These undulations do not coincide with Precambrian tectonic fabrics or crustal boundaries, hinting that they developed after crustal assembly and could instead reflect variable degrees of thinning, underplating, or crustal delamination during failed Proterozoic rifting, or perhaps of crustal buckling associated with the Grenville collision.

## 1. Introduction

North America's craton, the relatively stable portion of the continent that has not undergone orogenic deformation for > 1 billion years, can be divided into two provinces: the Canadian Shield, where bedrock at the ground surface consists of Precambrian crystalline basement, and the cratonic platform, the region in which Phanerozoic strata covers

basement. In comparison with Phanerozoic orogenic belts, land-surface topographic relief of the craton in the eastern midcontinent is subdued. Specifically, in our study area (Fig. 1), a portion of the eastern mid-continent lying between 39° and 48°N latitude and between 268° and 284°W longitude, the cratonic platform surface includes the interior plains, hosting elevations of < 300 m and relief of < 30 m, the fluvially dissected Appalachian Plateau, hosting elevations of < 980 m and relief

\* Corresponding author at: Department of Earth Science and Environmental Change, University of Illinois Urbana-Champaign, IL, USA.

E-mail address: [xiao.d.song@gmail.com](mailto:xiao.d.song@gmail.com) (X. Song).

of < 300 m, and a portion of the southern Canadian Shield that hosts elevations < 450 m and relief of < 100 m. Not only is this topographic relief much less than that of Phanerozoic orogenic belts, but it is also substantially less than structural relief of the Great Unconformity, the contact between Precambrian basement and Phanerozoic strata beneath the cratonic platform. Due to local Proterozoic rifting, Paleozoic epeirogenic displacements (broad, regional-scale vertical movements), and flexural loading by Phanerozoic orogens, the Great Unconformity of the cratonic platform in our study area displays relief of up to 7.5 km (Marshak et al., 2017). Significantly, the structural relief of the Moho beneath the cratonic platform is up to two to three times that of the Great Unconformity (Shen and Ritzwoller, 2016; Yang et al., 2017).

The above generalizations emphasize that, in contrast to contemporary collisional orogenic belts, variations in Moho depth and, therefore, in crustal thickness of the craton do not uniformly correlate with either land-surface relief or Great Unconformity relief (Table 1). In fact, the relationship between crustal-thickness variation and upper-crustal structure and contemporary topography in cratonic-platform regions remains unclear. The generalized map of Moho depth beneath the United States, that Shen and Ritzwoller (2016) produced, serves as a valuable foundation for studies of crustal-thickness variation. But the resolution available on that map cannot permit analysis of associations between known upper crustal structures and crustal thickness. Their study focused on the entire contiguous United States and exclusively utilized USArray Transportable Array (TA) broadband seismometers, which have an interstation spacing of approximately 70 km.

To remedy the lack of higher-resolution data on Moho depth in the northern Midcontinent region of the United States, Yang et al. (2017) used receiver functions with common conversion-point stacking to analyze a portion of the seismic data from EarthScope arrays and Flexible arrays that had been deployed in the Midcontinent from 2011 to 2015. From these results, they produced a higher-resolution map of Moho-depth variation for the Illinois Basin, Ozark Plateau, and adjacent regions. Yang et al. (2017)'s work implied that Moho depth varies by as much as 27 km across their study area, particularly in southern Illinois Basin, and that transitions between thicker and thinner crust are abrupt in some locations. Notably, a few of the abrupt transitions coincide with known upper-crustal structures. For example, the fairly abrupt boundary

**Table 1**

Estimated average crustal thickness of major structure features in the research area.

Structural Feature	Average Crustal Thickness	Standard Deviation
Canadian Shield	37.1 km	2.5 km
Michigan Basin	38.7 km	2.5 km
Wisconsin Dome	> 41 km	3.2 km
Kankakee Arch	39.3 km	0.9 km
Cincinnati Arch	37.6 km	3.3 km
Finlay Arch	> 43 km	1.8 km
western Appalachian Basin	> 43.8 km	2.3 km

between the relatively thin crust (beneath the Ozark Dome) and relatively thick crust (beneath the western Illinois Basin) coincides with the seismically active Ste. Genevieve fault zone of Missouri.

The Yang et al. (2017) study demonstrates that higher-resolution studies enabled by increased station density, have the potential to provide insights into the tectonic significance of cratonic Moho depth variations. Their study also implies that the Moho, at least locally, has a significant slope. As demonstrated by Li et al. (2019), the occurrence of dipping Moho surface leads to greater uncertainty in H- $\kappa$  stacking results ( $H$  stands for Moho depth and  $\kappa$  stands for  $V_p/V_s$  ratio) of receiver-functions stacking analysis. To reduce the uncertainty induced by a dipping Moho and/or crustal anisotropy in H- $\kappa$  stacking, Li et al. (2019) proposed a modified stacking method, called the H- $\kappa$ -c method (c stands for "corrected"). They first performed a moveout correction, followed by applying trigonometric functions to receiver functions to accommodate for dipping boundaries.

While the H- $\kappa$ -c method can reduce uncertainty in crustal thickness estimates, alternative approaches also exist for obtaining crustal thickness from receiver functions. For example, Sadler and Pulliam (2023) use RFs and autocorrelations to estimate both sedimentary basin depth and Moho depth without relying on a fixed  $V_p$ , while Wang et al. (2021) incorporate data from nearby stations to automatically interpret interfaces. We ultimately chose the H- $\kappa$ -c method for its consistency and ability to refine the crustal thickness estimates in our study.

The H- $\kappa$ -c method decreases the uncertainty of crustal-thickness estimations and has been applied in various geological settings, including

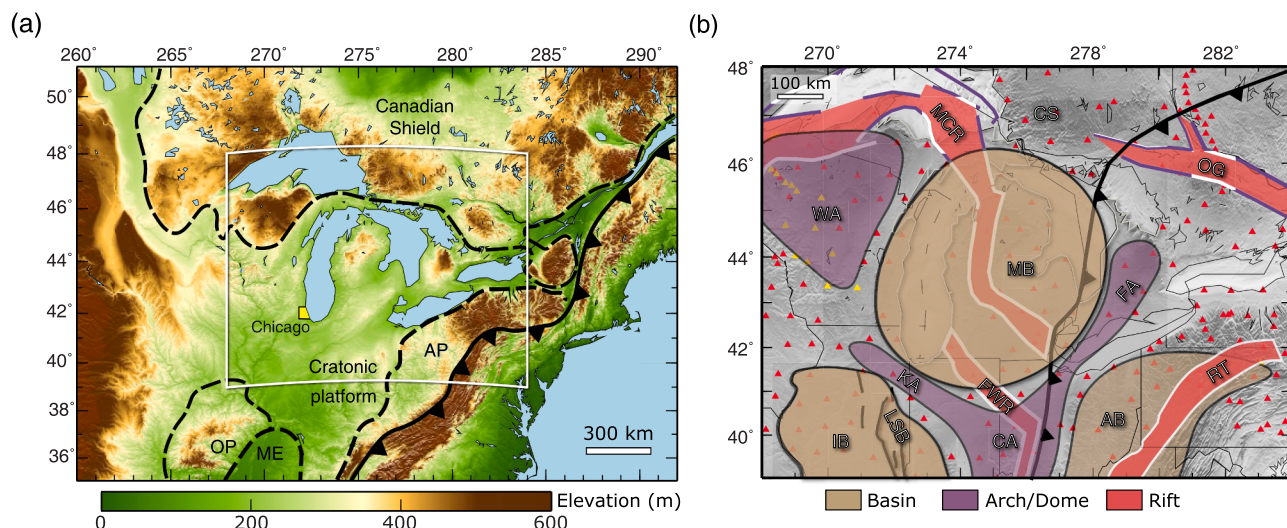


**Fig. 1.** (a) Physiography of the study area (white rectangle) as enhanced on a NASA shaded relief map. Colors symbolize elevation (greens are lower elevation, tans are higher elevation). Note that the study area encompasses portions of the interior plains, intracratonic plateaus, and the Canadian Shield. The solid front represents the Appalachian Front. The dashed line delimits the major geological provinces. AP = Appalachian Plateau; OP = Ozark Plateau; ME = Mississippi embayment. (b) Regional structural features and seismic station distribution on a digital elevation model of the area. Tan areas indicate major basins, and purple areas indicate major arches (simplified from Marshak and van der Pluijm, 2021). Red areas indicate major rifts (from Stein et al., 2018). IB = Illinois Basin; LSDB = La Salle Deformation Belt; CA = Cincinnati Arch; FWR = Fort Wayne Rift; AB = Appalachian Basin; RT = Rome Trough; KA = Kankakee Arch; FA = Findlay Arch; MB = Michigan Basin; WA = Wisconsin Arches; MCR = Midcontinent Rift; CS = Canadian Shield; OG = Ottawa Graben. Seismic-station localities are indicated by the small triangles. Stations with robust H- $\kappa$ -c estimates are red, and the stations with receiver function coverage gaps are in yellow.

Tien Shan (Zhang et al., 2020), Tibetan Plateau (Li et al., 2021), South China (Deng et al., 2019), and central mid-continent (Xiao et al., 2022). Higher-resolution Moho estimates are achieved with densely distributed stations using the H-k-c method. For instance, the SPREE Array has an average station spacing of approximately 12 km, compared to the 70 km spacing of the TA Array. The inclusion of all available stations within our study area, along with the increased station density, significantly enhances the resolution of the Moho estimates.

Xiao et al. (2022) used the H-k-c method to reevaluate crustal thickness beneath the Ozark Dome and southern Illinois Basin region. Their results confirmed the general depth variations by Yang et al. (2017), but indicated that the contrast in crustal thickness across the Ste. Genevieve fault is somewhat less than the contrast proposed by Yang et al. (2017). Also, Xiao et al. (2022) showed that Moho depth "undulates" (varies in depth) at two wavelengths; "long-wavelength undulations" display a crest spacing of approximately 160 km, whereas "short-wavelength undulations" display a crest spacing of approximately 60 km. Both types of undulations have wave heights (trough to crest) on the order of 15 km. Notably, short-wavelength undulations were visible only in areas where seismic stations were densely spaced (i.e., in the area of EarthScope's OIINK flexible array).

Previous studies' (Xiao et al.'s, 2022; DeLucia et al., 2019; Murphy et al., 2024), results prompt several questions: (1) Do short-wavelength undulations occur throughout the craton of the eastern Midcontinent?; (2) Do long-wavelength undulations occur widely and, if so, do they display a recognizable pattern?; (3) Do trans-crustal shear zones boundaries between Precambrian tectonic provinces, and/or known rifts correlate with crustal thickness variations?; (4) Do other basins, such as the Michigan Basin and the Appalachian Basin, have the same crustal thickness as the Illinois Basin? To address these questions, we apply the H-k-c method to obtain a higher-resolution image of Moho-depth beneath a portion of the eastern Midcontinent north and east of the area studied by Xiao et al. (2022).

Our new results demonstrate that crustal thickness variations of about twice that of the Great Unconformity's relief occur throughout the cratonic platform of our study area, comparable to the long-wavelength undulations discussed by Xiao et al. (2022). (We could not detect short-wavelength undulations, because no dense flexible arrays have been deployed in the region.) In general, crust is thicker beneath basins than beneath domes and arches, but this pattern does not occur everywhere. Notably, crustal thickness beneath the Michigan Basin is less than that beneath the Illinois Basin, indicating that intracratonic basins do not necessarily share the same crustal structure. Crustal thickness variations locally correlate with upper-crustal structures, as exemplified by the alignment of a belt of relatively thin crust with a portion of the Midcontinent Rift in Michigan. Of particular interest, we detected several north-south-trending undulations, with wavelengths of about 150 km, in the northern half of our study area, mostly west of the Grenville front. The trend of these undulations does not correlate with Proterozoic tectonic boundaries, implying that they developed after crustal assembly.

## 2. Geologic context of the study region

Our study area (from latitude 39°N to 48°N, to longitude 268°W to 284°W) encompasses the northern Midwest of the United States, the adjacent portion of southern Canada and part of the neighboring Appalachian foreland. This region includes a portion of North America's cratonic platform as well as a portion of the Canadian Shield. In the cratonic platform, Precambrian basement rock remains buried by Paleozoic cover strata, whereas in the Canadian Shield, basement crops out at the ground surface. The Great Unconformity, a widespread erosional surface that formed during late Precambrian exhumation, serves as the boundary between basement and cover. The trace of the Great Unconformity on the ground surface delineates the map boundary between the platform and the shield.

The basement of the cratonic platform in the study area formed by the suturing together of crustal slivers and blocks, as well as by formation of volcanic arcs and other igneous provinces during convergent-accretionary tectonism that took place between 1.8 and 1.6 Ga. This amalgamation yielded the northeast-trending Yavapai and Mazatzal belts (Karlstrom and Humphreys, 1998; Van Schmus et al., 2007; Shaw and Karlstrom, 1999). Between 1.5 and 1.3 Ga, extensive felsic igneous activity overlapped portions of the Yavapai and Mazatzal belts and generated the Eastern Granite-Rhyolite Province (Bickford and Van Schmus, 1985). The 1.45 Ga Picuris Orogeny also deformed and metamorphosed part of the Midcontinent's crust (Fig. 2; Daniel et al., 2023). Multiple stages of the Grenville Orogeny occurred between about 1.2 and 0.9 Ga (e.g., Gordon and Hempton, 1986). During the Grenville Orogeny, new crustal blocks docked along the eastern margin of Laurentia (the combined crust of North America and Greenland), and a major continental collision took place, forming a broad belt of penetrative metamorphism and deformation whose western boundary today is the Grenville Front, a shear zone which trends north-south to northeast-southwest across our study area (Li et al., 2008). When the Grenville Orogeny was complete, Laurentia had become part of the Rodina supercontinent.

Major rifting events affected the Midcontinent of our study area two or more times. The Keweenawan rifting event, at about 1.1 Ga, appears to have occurred between stages of the Grenville orogeny (e.g., Gordon and Hempton, 1986). It produced the Midcontinent Rift, which locally filled with up to 15 km of basalt and stands out as a prominent gravity anomaly (e.g., Stein et al., 2014). The main arm of the Midcontinent Rift underlies Lake Superior and can be traced beneath Minnesota and Iowa to Kansas (Behrendt et al., 1989; Hinze and Chandler, 2020). The eastern arm underlies the Michigan Basin. Iapetan rifting occurred at the end of the Proterozoic, in association with the breakup of Rodinia, and yielded the Reelfoot Rift and Rome Trough as well as normal or numerous transtensional faults in regions between distinct rifts (Moecher et al., 2018). Our study area includes several known rifts (the eastern Mid-Continent Rift, the Fort Wayne Rift, the central Rome Trough, the La Salle Belt, and the Ottawa Graben). During and/or following rifting, widespread intense erosion stripped away as much as the top few kilometers of the crust, producing the Great Unconformity. (DeLucia et al., 2018)

During the Paleozoic, several phases of transgression and regression deposited sequences of platform strata in the Midcontinent (e.g., Sloss, 1988). Differential epeirogenic subsidence and uplift, took place in pulses during the Paleozoic and caused significant regional variation in the thickness of Phanerozoic strata. Epeirogenic movements producing broad (> 300 km across) intracratonic basins and domes, as well as narrower (< 100 km across) elongate intracratonic arches (e.g., Marshak and van der Pluijm, 2021). Strata are thicker in the interior of basins than at the crests of domes and arches. For example, the Michigan Basin is nearly circular in shape and reaches a depth of approximately 5 km at its center (Leighton, 1996). Along the eastern margin of the study area lies the Appalachian Basin, which may have initially formed as an intracratonic basin over the Rome Trough, an Iapetan rift. At the end of the Paleozoic, the basin experienced significant subsidence during the development of the late Alleghenian fold-thrust belt. The emplacement of thrust sheets caused flexural downwarping of the North American lithosphere, which further amplified the subsidence of the basin. Strata in these basins thin near the flanks of arches and domes.

Numerous fault-and-fold zones, some of which represent inverted rifts (e.g., the La Salle Belt in the Illinois Basin), occur within epeirogenic structures or form borders between epeirogenic structures (Fig. 1b). Marshak and Paulsen (1997) suggested that these faults initially formed as normal or transform faults during Proterozoic rifting, for some of them border documented rifts or define cross-strike steps in the rifts. Notably, two main sets of faults occur, one trending west to northwest and the other trending north to northeast; these trends roughly parallel the trends of documented rifts. The faults have undergone reactivation,

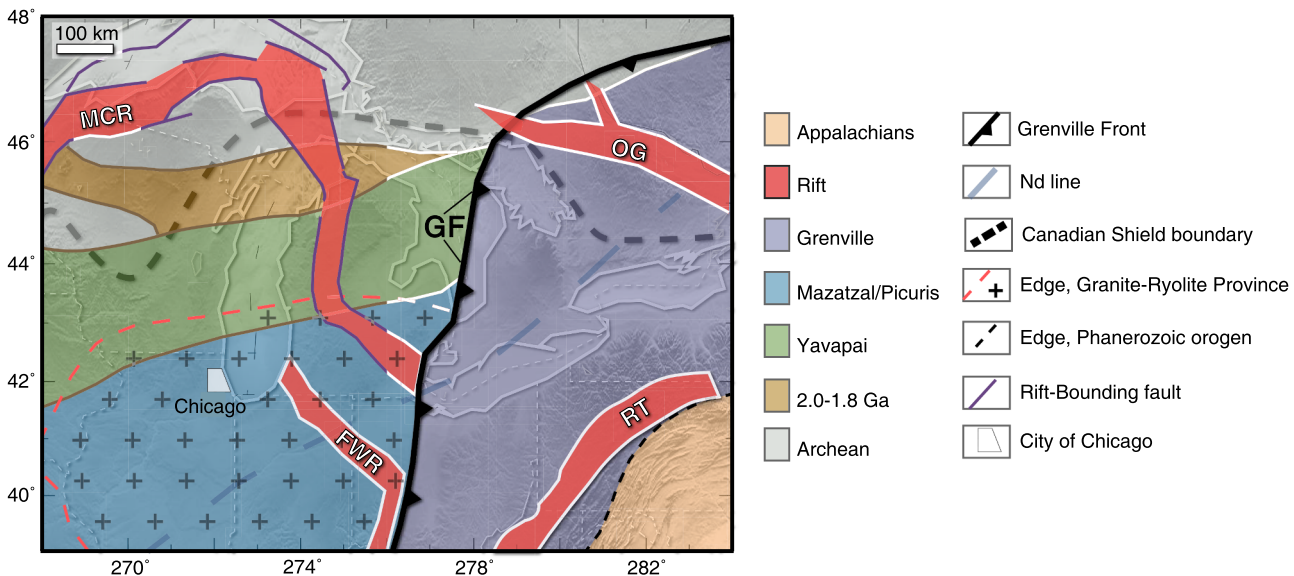


**Fig. 2.** Major geological boundaries in the research area (simplified from Marshak and van der Pluijm., 2021). MCR = The Midcontinent Rift; GF = Grenville Front; OG = Ottawa Graben; FWR = Fort Wayne Rift; RT = Rome Trough.

as transpressional structures, episodically during the Paleozoic, and some remain seismically active today (e.g., Marshak and van der Pluijm., 2021).

### 3. Methods

The traditional H- $\kappa$  stacking method uses converted waves (P to S conversions that take place at the Moho) to estimate both Moho's depth and the  $V_p/V_s$  ratio underneath a seismic station (Zhu and Kanamori, 2000). Significantly, this stacking assumes that seismic velocity contrast interfaces, such as the Moho, are relatively flat-lying, and the crust is relatively homogeneous. Consequently, in areas where the Moho dips, or in places where crust is not homogeneous, Moho-depth estimates obtained using the traditional H- $\kappa$  stacking can result in estimates that have substantial uncertainty. To overcome this problem, and reduce uncertainty, we used the H- $\kappa$ -c method developed by Li et al. (2019), which uses  $\cos\theta$  and  $\cos 2\theta$  functions to fit Ps phase and its crustal multiples, with respect to back azimuth ( $\theta$ ), the angle measured clockwise from north to the event epicenter from the station. The calculation realigns the Ps phase and its crustal multiples (M1, meaning PpPs, and M2, meaning PpSs+PsPs) to their central arrival time. For simplicity, we will refer to Ps, M1, and M2 as the “targeted phases.”

The harmonic fitting curve uses the following equation for the grid search and corrections (Li et al., 2019):

$$F(\theta) = A_0 + A_1 \cos(\theta - \theta_1) - A_2 \cos 2(\theta - \theta_2), \quad (1)$$

where  $A_0$  is the central arrival time, and  $A_1$ ,  $A_2$  and  $\theta_1$ ,  $\theta_2$  are the amplitudes and phases of the two-lobed and four-lobed variations. Simplistically in end-member scenario,  $A_1$  and  $\theta_1$  represent dip parameters, and in another end-member scenario,  $A_2$  and  $\theta_2$  represent anisotropy (fast axis) parameters. Li et al. (2019) provide details about the parameters and tested scenarios.

For a given data set, the H- $\kappa$ -c computer program first performs a grid search on the radial receiver functions (R-RFs) to find the best solutions for search parameters (such as  $A_0$ ,  $A_1$ ,  $A_2$ ,  $\theta_1$ ,  $\theta_2$ ). For each search, it first computes a harmonic curve according to Eq. (1). Then, it aggregates the amplitudes of receiver functions at every point on the harmonic curve. It will then iterate with different parameter solutions that have a different sum of the amplitudes. Ultimately, the H- $\kappa$ -c program considers the parameters that have the largest sum of amplitudes on the harmonic curve to be the optimal solution. Where the Moho has a significant dip,

the receiver functions calculated at different back azimuths have different arrival times for specific targeted phases. Using the optimal solution from previous calculations, the H- $\kappa$ -c method realigns all targeted phases, one by one, to their central arrival time ( $A_0$ ), by using the harmonic functions. Finally, the H- $\kappa$ -c method program performs H- $\kappa$  stacking using the corrected receiver functions to estimate H (crustal thickness) and  $\kappa$  ( $V_p/V_s$  ratio). The H- $\kappa$ -c method, therefore, reduces uncertainty.

Before carrying out the calculations (such as deconvolutions, stacking, and parameter searches) described above, all data in our study first needed to be preprocessed. To do this, we first retrieved the BHE (broadband east/west), BHN (broadband north/south), and BHZ (broadband vertical) channel time series data from the EarthScope SAGE Data Management. Then we trimmed the waveform to 50 s before the first P arrival and 150 s after the first P arrival. A bandpass filter with 0.05 Hz to 2 Hz was applied to the waveforms then the filtered waveforms were resampled to 10 samples per second and rotated to the RTZ (radial, transverse, and vertical) system. Then, we followed Li et al.'s (2019) processing procedures on all stations. We first used the traditional H- $\kappa$  stacking method to generate a reference Moho depth for each station. Then we used this reference Moho depth to guide the search for parameters to correct targeted phases during H- $\kappa$ -c method. We adopted the same weighting scheme as Li et al. (2019), using relative weights of 0.7 for Ps, 0.2 for M1, 0.1 for M2 and a  $V_p$  value of 6.3 km/s in H- $\kappa$  stacking (Zhu and Kanamori., 2000), and 0.5, 0.4, and 0.1 in H- $\kappa$ -c stacking. The weighting adjustment accounts for the improved coherency of the M1 phase after correction (Li et al., 2019).

For our study, we analyzed data from a well-balanced distribution of 228 broad-band stations (see Fig. 1b). Of these, 130 were part of the USArray Transportable Array, 77 were from regional networks (such as the N4 network), and 11 were from permanent or long-term stations (Table S1). Our study was limited to records of earthquakes that had magnitudes greater than or equal to  $M_w$  5.0, occurred at distances between 30° and 95° from the recording stations, and took place between January 1995 and March 2019. Notably, waveform data from regional networks were only available for the limited time range determined by each station's deployment time. Given these restrictions, our initial data set included 18,011 events. However, for the H- $\kappa$ -c method to work effectively, and yield a unique result, each station used must have at least one receiver function per 90° azimuth (Li et al., 2019). Most of the stations with more than 2 years' worth of data did have such azimuthal

coverage, but a few of them do not. To test the stability of solutions provided by the H- $\kappa$ -c method correction, we varied the reference Moho depth from 30 km to 70 km during the parameter grid search in H- $\kappa$ -c. We only kept results that remained consistent despite changes in the reference values.

To demonstrate how the H- $\kappa$ -c method decreases the uncertainty of depth and Vs/Vp data, obtained from receiver functions, as compared to the H- $\kappa$  method, we provide an example using data from Station N58A (Fig. 3). This station, part of the TA array (of USArray), lies in Western Appalachian Basin. Each column in Fig. 3 provides data for one of the three targeted phases from Station N58A (left = Ps; center = M1; right = M2). Fig. 3a provides close-up images of receiver-function records, plotted by their back-azimuths; each trace includes multiple events that are binned every 5°. The first column proved Ps for the interval between 3s and 8s, the center column represents M1 phase for the interval between 13s and 18s, and the third column represents M2 phase for the interval between 19s and 24s. These are the records that were subsequently used in the parameter search to maximize the sum of Eq. (1) over all back azimuths. Fig. 3b illustrates the parameter search results for N58A for Ps, M1 and M2 phases. The Ps and M1 phases primarily contribute to resolving crustal thickness and Vp/Vs ratio, as they provide clear, coherent signals that enhance stacking accuracy. However, the M2 phase is more complex and less reliable due to crustal anisotropy and dip. Given its lower weight in H- $\kappa$  stacking, its influence on the final results is limited. For further details, please refer to Li et al. (2019). Fig. 3c–e provide energy maps ( $A_1$  vs.  $A_2$ ,  $\cos\theta$  term, and  $\cos 2\theta$  term), which are 2-D views of the 5-D parameter space. Each of the three energy maps in each column corresponds to a phase. The parameter combination that provides the maximum energy in each energy map is the optimal solution. Using the optimal solution, we use Eq. (1) to correct the receiver functions by shifting each phase to its central arrival time  $A_0$ . The solid black curves in Fig. 3a represent the best-fitting curve (optimal solution).

After the correction on each phase, the corrected time series were merged back together (Fig. 4a). Based on the results such as those of Fig. 3, we can produce an improved receiver-function stacking with a revised estimation of H and  $\kappa$ . For example, Fig. 4b shows the stacking produced by the original H- $\kappa$  method, while Fig. 4c shows the stack produced by the H- $\kappa$ -c method. Uncertainty is greatly reduced by using the H- $\kappa$ -c stacking method, as evident by comparing the uncertainty ellipse for the H- $\kappa$  estimate to the smaller ellipse resulting from application of the H- $\kappa$ -c method. Also, note that the depth of the Moho in Fig. 4c differs from that in Fig. 4b. Specifically, the H- $\kappa$  estimate for Moho depth is  $41.5 \pm 5.4$  km, while the H- $\kappa$ -c estimate for Moho depth is  $38.5 \pm 2.4$  km. The uncertainty of H was reduced from 5.4 km to 2.4 km and the uncertainty of  $\kappa$  was reduced from 0.1 in H- $\kappa$  to 0.06 after H- $\kappa$ -c correction.

## 4. Results

### 4.1. Data quality

We analyzed data from a total of 228 stations in this study. 34 stations of the stations were previously analyzed by Xiao et al. (2022). After the preprocessing described above, we ended up with reliable data from a total of 214 broad-band seismic stations.<sup>1</sup> Unfortunately, we could not retrieve the H- $\kappa$ -c correction estimates from all the stations for various reasons. Specifically, we excluded stations that had missing, inconsistent, or anomalous waveform data or documentation (e.g., some data of poor quality from the EarthScope SAGE Data Management); stations that did not have adequate azimuth coverage; and stations that did not converge on a stable solution for the harmonic correction (so that the H- $\kappa$ -c estimate could not yield a unique and reliable estimation).

<sup>1</sup> The details of each station are listed in Table S1.

Consequently, we were able to use the H- $\kappa$ -c method successfully for a total of 194 stations to obtain crustal thickness and Vp/Vs ratio. Data details and the errors are included in the supplementary materials (Table S1). Of note, we also included 16 stations (marked with yellow triangles on Fig. 1a) that did not have sufficient receiver function azimuth coverage for H- $\kappa$ -c correction. However, our testing revealed that the trigonometric correction parameters for these stations were stable. To test the stability of these stations' results, we varied the reference Moho greatly from 30 km to 70 km. We kept the consistent and stable estimates (16 stations) as the best estimates and discarded the rest.

We found improvement in both the H and  $\kappa$  estimates, as well as a reduction in the error range, for 181 out of 214 stations that were presented in this study. The results we describe below use only the stations with successful H- $\kappa$ -c estimates.

### 4.2. Crustal thickness variations

Our study (Fig. 5) shows that the average crustal thickness of the study area ranges from 34 to 47 km, with an overall average of 40.0 km. Additionally, we provide a Vp/Vs ratio map of the study area in the supplemental material (Fig. S2). Notably, the platform region averages around 41.7 km. In contrast, the Canadian Shield within the study area has a thinner crust averaging around 37.1 km. Within the cratonic platform region, there are distinct differences between different areas. For example: beneath the Michigan Basin, crustal thickness averages around 38.7 km; beneath the Wisconsin Arch, it has a thicker crust, with an average of 41.8 km; beneath the Kankakee Arch, the crustal thickness averages at 39.3 km, beneath the Cincinnati Arch, the average crustal thickness is 37.6 km; and beneath the Finlay Arch, the average crustal thickness is 43.5 km. The crust beneath western Appalachian Basin is notably thicker than the Michigan Basin, for the crust beneath the Appalachian Basin averages greater than 43.8 km. The Michigan Basin crust is also significantly thinner than that of the Illinois Basin, for results reported by Xiao et al. (2022) indicate that crust beneath the Illinois Basin ranges from 45 to 57 km. Detailed variations in crustal thickness in the Michigan Basin suggest that there is a relationship between crustal thickness and part of the eastern arm of the Midcontinent Rift, in that the crust is thinner beneath the rift than along its border. Also of note, the crust of the northern half of the Michigan basin is notably thinner than that of the southern half. Results in Xiao et al. (2022) also show that the arches of the study area have crust that are comparable to that of the Ozark Dome.

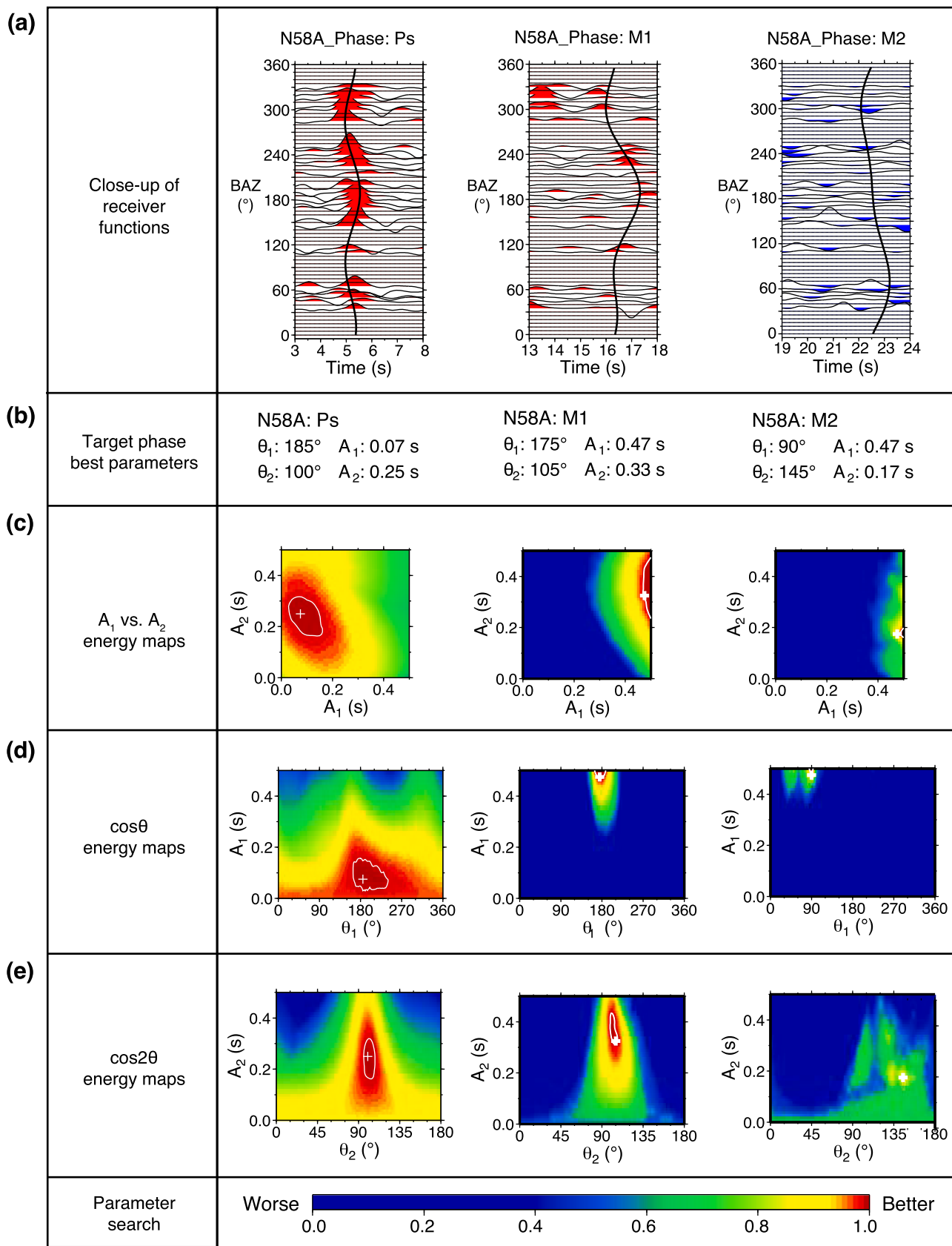
Fig. 5 displayed an unexpected result. In the region west of the Grenville Front in the cratonic platform, and beneath the Canadian Shield in our study area, Moho depth displays somewhat systematic undulations. Specifically, the map suggests that north-south-trending bands of thicker crust, that are about 150 km wide, alternate with comparable bands of thinner crust. Moho depth varies from 43 km to 37 km and back to 43 km over a horizontal distance of about 150 km (Fig. 6; Xiao et al., 2022). In other words, the north-south trending undulations of Moho display a wavelength of a little over 1° at 42°N latitude, and an amplitude of about 7 km. Such undulations are not prominent beneath the Appalachian basin or beneath the southern Illinois Basin.

$\kappa$  values display a similar north-south banding pattern similar to crustal thickness and are generally high with a mean of 1.79 over the entire region (Fig. S2 and Table S1 in Supplementary materials). This pattern does not align with the pre-Cambrian fabric. The average is more like those (1.73–1.80) obtained also from the improved H- $\kappa$ -c method for an active tectonic region such as the Tibetan Plateau (Li et al., 2019; Li and Song, 2021).

## 5. Discussion

### 5.1. Patterns of crustal thickness variations

We used the H- $\kappa$ -c receiver-function method to calculate refined



(caption on next page)

**Fig. 3.** An example of H-k-c correction results for a Station N58A. Each column is for a different targeted phase. (a) Ps phase receiver functions records from 3s to 8s plotted by their back-azimuths. M1 phase receiver functions records from 13s to 18s plotted by their back-azimuths. M2 phase receiver functions records from 19s to 24s plotted by their back-azimuths. Note that each receiver function trace includes multiple events that are binned every  $5^\circ$ . The solid black curves in each subpanel represent the best-fitting curve (optimal solution) for Ps / M1 /M2 respectively. (b) An illustration of the parameter search results for N58A for Ps, M1 and M2 phases respectively. (c) Energy maps ( $A_1$  vs.  $A_2$ ) of the parameter search results for Ps, M1 and M2 phases respectively. Energy maps are 2-D views of the 5-D parameter space. Three energy maps in each column correspond to three targeted phases (Ps, M1 and M2). For each column, parameter search finds the crosses (optimal solution) in energy map, which will have largest sum over all azimuths based on Eq. (1). From Li et al. (2019),  $F(0) = A_0 + A_1 \cos(\theta - \theta_1) + A_2 \cos^2(\theta - \theta_2)$ , where  $A_0$  is the central arrival time and  $A_1, A_2$  and  $\theta_1, \theta_2$  are the amplitudes and phases of the two-lobed and four-lobed variations. Back azimuth is denoted by  $\theta$ . (d) Energy maps ( $A_1$  vs.  $\cos\theta$  term) of the parameter search results for Ps, M1 and M2 phases respectively. (e) Energy maps ( $A_2$  vs.  $\cos 2\theta$  term) of the parameter search results for Ps, M1 and M2 phases respectively.

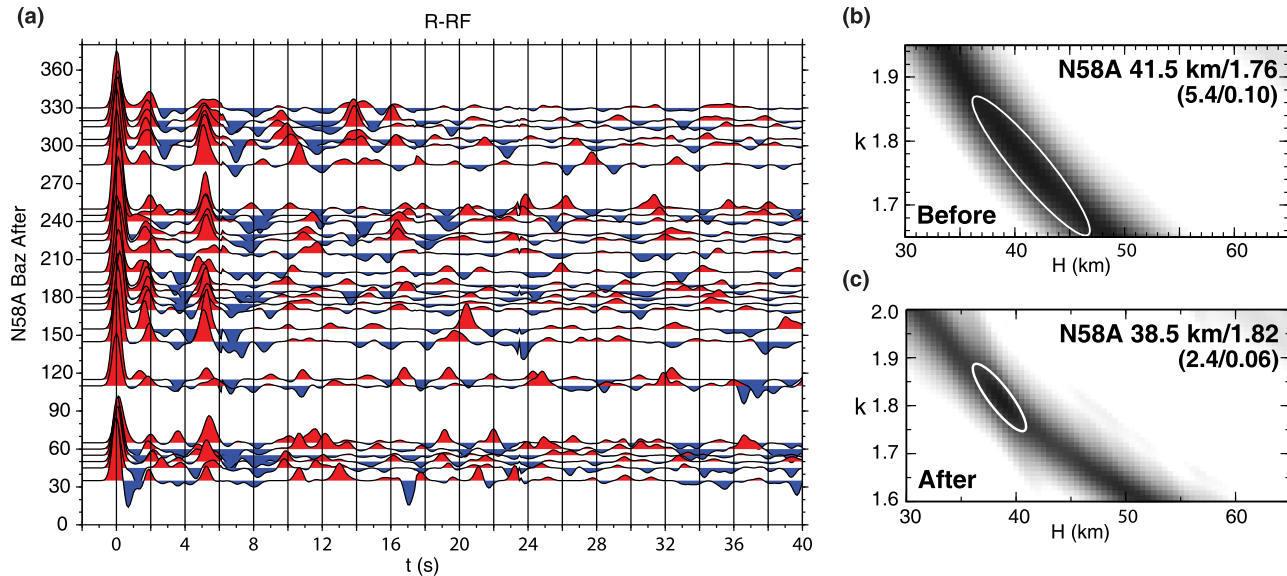


**Fig. 4.** Comparison of results from traditional and corrected stacking procedures for Station N58A. (a) Record sections after H-k-c correction. Receiver functions were sorted by azimuth (grouped every  $5^\circ$ ). (b) The stacking result of H (representing crustal thickness) and  $\kappa$  (representing Vp/Vs ratio) using uncorrected receiver functions, numbers in the parenthesis are uncertainty value for H and  $\kappa$  respectively. (c) The stacking result of H vs.  $\kappa$  after the H-k-c correction. Note that the uncertainty ellipse is much smaller than in 'c'. The values in the corners of panels b and c (within parentheses) represent Moho depth uncertainty and Vp/Vs ratio uncertainty, respectively.

Moho-depth estimates, which have smaller uncertainties compared to those available in earlier studies, for the eastern Midcontinent of North America. Within the study area, crustal thickness ranges from 34 km to 47 km. Therefore, crust beneath this portion of North America's craton varies by as much as 13 km. Variations of such magnitude or more have been observed beneath Phanerozoic orogens and rifts, but have not been widely recognized beneath cratonic crust. For instance, in the North China Craton, a 7 km Moho relief contrast was observed beneath the Ordos Basin (Gao et al., 2022; Li et al., 2022). Additionally, according to the Crust 1.0 model (Laske et al., 2013), Moho depth is 35 km greater beneath the Himalayas and Tibet, relative to that beneath the Indian Shield. Therefore, Moho relief across the Cenozoic-age Himalayan collision zone is about 2.7 times that beneath the craton of our study area; in other words, relief of the cratonic Moho in our study area is about 37 % of the relief across the Indian Craton - Himalayan Orogen boundary. Similarly, according to Crust 1.0, Moho relief between the East African Rift and the African craton is about 10 to 20 km, comparable to the relief between our study area. Notably, land-surface topographic relief between the Indian Craton and the Himalayan orogen is about 5 km (up to 8.5 km), whereas the relief in our study area is about 0.5 km (up to 0.7 km). Therefore, the ratio of Moho relief to topographic relief is about 3.5 times greater beneath the craton than in the transition from the craton to the Himalayan Orogen. Relief on the Great Unconformity (GU) is a maximum of about 7.5 km. Therefore, Moho relief contrast is about twice that of relief on the GU.

The variations in Moho depth (Fig. 5) indicate that the Moho of southern Canadian Shield is, on average, shallower than the Moho depth

beneath the cratonic platform. Further, we note that places in the platform where Paleozoic sedimentary cover is thinner (namely, arches and domes), with some exceptions, are regions where the crust is thinner. This observation hints that crustal thickness plays a role in determining whether a region of crust epeirogenic subsidence or not, and whether the region persists as a cratonic platform region instead of becoming a shield. This generalization, however, does not appear to apply everywhere. Specifically, while relatively thick crust underlies the western Appalachian Basin and the Illinois Basin, relatively thin crust underlies the Michigan Basin. Similarly, while relatively thin crust underlies the Cincinnati Arch, the Kankakee Arch, and the Ozark Dome, in contrast, relatively thick crust underlies the Wisconsin Arch and the Findlay Arch.

In the Himalayan orogen, higher land-surface topography correlates with thicker crust. Such a correlation does not apply in the cratonic platform area of our study area. Specifically, the relatively higher topography of the Ozark Plateau occurs in a region of relatively thinner crust, whereas relatively lower topography of the Illinois Basin occurs in a region of thicker crust.

Our results also indicate that the Grenville Front does not uniformly mark the boundary between zones of different crustal thickness (Fig. 5). Specifically, the Grenville Front overlies thinner crust in the region north of the eastern arm of the Midcontinent Rift, but overlies thicker crust in the region to the south.

Locally, variations in crustal thickness correspond with known upper crustal fault zones. For example, the Ste. Genevieve Fault Zone in eastern Missouri lies near the abrupt step between the thin crust of the St. Francis Mts. in the northeastern Ozark Plateau, and the Sparta Shelf

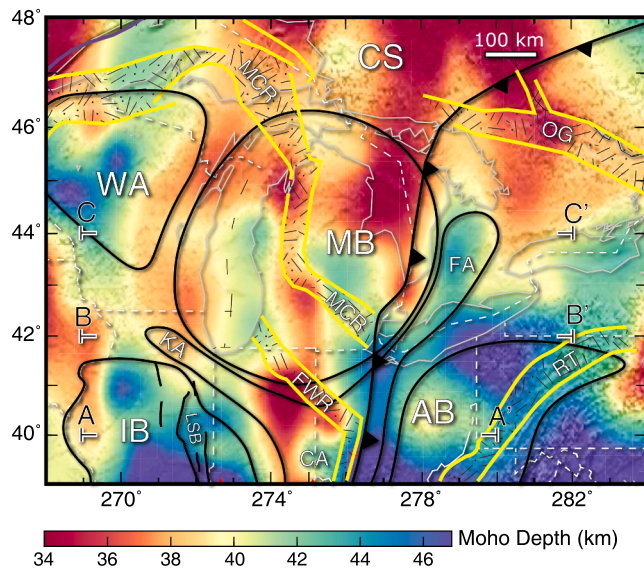


**Fig. 5.** (a) Variations in crustal thickness in the eastern midcontinent of the United States and adjacent Canada. This map is based on contouring Moho depth results, calculated using the H- $\kappa$ -c method, from 228 stations. Depth variations are displayed by using the “surface” function in GMT (Wessel and Smith, 1998). (b) This is the same map as in ‘a’, but on this map we highlight key structural features using solid grey lines and show the locations of the profiles provided in Fig. 6. The abbreviations are the same as those used in Fig. 1.

of the western Illinois Basin (Xiao et al., 2022), and the Kankakee Arch aligns with the Sandwich Fault zone of Illinois. Similarly, much of the eastern arm of the Mid-Continent Rift overlies a belt thinner crust within the Michigan basin, and the LaSalle deformation belt of Illinois overlies a relatively thinner crustal band in the Illinois Basin.

The overall pattern of crustal thickness variations, visually defined by undulations in the Moho depth, do not correlate with major Proterozoic terrane boundaries (see Fig. 2). Specifically, slopes in basement topography do not align with the boundary between the northeast-trending Yavapai and Mazatzal belts or with the Nd-line. In fact, the distinctive north-south-trending alternating belts of thicker and thinner crust in the northern half of our study area cut across both Mesoproterozoic terrane boundaries and Neoproterozoic rifts.

## 5.2. Possible explanations for crustal thickness variations

Several phenomena have been proposed to explain crustal thickness variations in the craton (e.g., Yang et al., 2017). These include:

- (1) *Inheritance from the Proterozoic assembly of crustal blocks:* If different crustal blocks had different thicknesses prior to assembly, or underwent different amounts of horizontal shortening and vertical thickening during assembly, or underwent different amounts of imbrication or duplexing during assembly, crustal thickness variations could have remained when assembly was complete, and could have been preserved by cratonization. Such variations have been observed in central Tibet (Chen and Jiang, 2020) and northeast Asia (Wang et al., 2017). This explanation seems less likely to apply to our study area, as the thickness variations we observed are not parallel to structural trends within the accretionary orogens.
- (2) *A consequence of post-assembly faulting:* Trans-crustal faults have been observed in orogens, where they produce crustal thickness variations. But in such situations, slip on the faults produced substantial displacement. There is no evidence indicating that significant vertical throw occurred on faults in the eastern craton

subsequent to assembly. Specifically, Paleozoic transgressive faults, many of which represent inversion of Proterozoic normal faults (Marshak and Paulsen, 1996), of the region display relatively little vertical displacement, less than necessary to explain crustal thickening. Conceivably, upper-crustal faults active during Neoproterozoic and Early Paleozoic rifting linked to normal-sense shear zones at depth that accommodated lower-crustal extension, and such extension does not necessarily underly belts of upper-crustal extension (Fig. 7a; e.g., Lister et al., 1986; Clerc et al., 2018), however, this model remains untested due to the lack of a feasible approach.

- (3) *Post-assembly mafic igneous activity (differential underplating):* As we noted earlier, igneous activity accompanied pulses of Proterozoic rifting. As documented in several locations (McGlannan and Gilbert, 2016; Medaris et al., 2021; Thybo and Artemieva, 2013), underplating of the crust, and intrusion of the lower crust, by basaltic sills typically accompanies rifting. Such igneous activity may explain some of the crustal thickness variations that we observed (Fig. 7a). For example, rift-related underplating has been proposed as a mechanism to thicken crust beneath the Michigan Basin (e.g., Stein et al., 2018) and the Illinois basins (McBride et al., 2016; Yang et al., 2017; Xiao et al., 2022). But most of the thickness variations that we observed are not spatially associated with known rifts. So, either such igneous activity does not explain the crustal-thickness variations that we observed, or such activity occurred even where upper-crustal extension did not develop.
- (4) *Post-assembly felsic igneous activity:* Large areas of our study area are within the Eastern Granite Rhyolite Province. If the production of felsic magma, and presumably mafic magma at depth, is inhomogeneous, it might contribute to variations in crustal thickness. The volumes involved would be immense.
- (5) *Differential Delamination:* Differential lower-crustal thinning can be a consequence of delamination of lower crust (e.g., Kay and Kay, 1993; Meissner and Mooney, 1998; Lustrino, 2005). Such delamination can occur where the mafic rocks of the lower crust have undergone eclogitization, and therefore are dense enough to sink into the asthenosphere (Fig. 7b). Conceivably, at times when a large plume develops beneath the lithosphere, the lithospheric mantle thins sufficiently for the asthenosphere to rise to the base of the lower crust. Heat transfer from the plume could weaken the lower crust, and would make the underlying mantle less viscous. Such change in material properties could allow lenses of eclogitized lower crust to delaminate. In North America, evidence for delamination has been found beneath the southern Sierra Nevada (Zandt et al., 2004), and the concept has been applied to the craton (Yang et al., 2017). Such delamination was also proposed in the North China Craton during the early Paleoproterozoic along with rifting (Liu et al., 2020).
- (6) *Lithospheric buckling:* Cloetingh and Burov (2011), Tikoff et al. (2022) have suggested that the entire crust, or even the lithosphere, may undergo buckling in response to collisional stresses. In concept, the lithosphere can be viewed as a relatively rigid layer sandwiched between less rigid layers. Tikoff et al. (2022) suggest that buckling of the lithosphere could produce folds with amplitudes on the order of 150 km. This is comparable to the wavelength of the 7 km-amplitude undulations that we observed in the northern part of our study area. The spatial association of these with the Grenville front hints that they could have developed in response to compressional stress during the Grenville orogeny.
- (7) *Misinterpretation of the Moho:* In our study we recognized the Moho as a distinct boundary across which an abrupt velocity change takes place. As shown in Fig. 4, our H- $\kappa$ -c results provide a smaller uncertainty ellipse, thereby increasing our confidence in our picks for Moho depth. Of course, we cannot rule out the

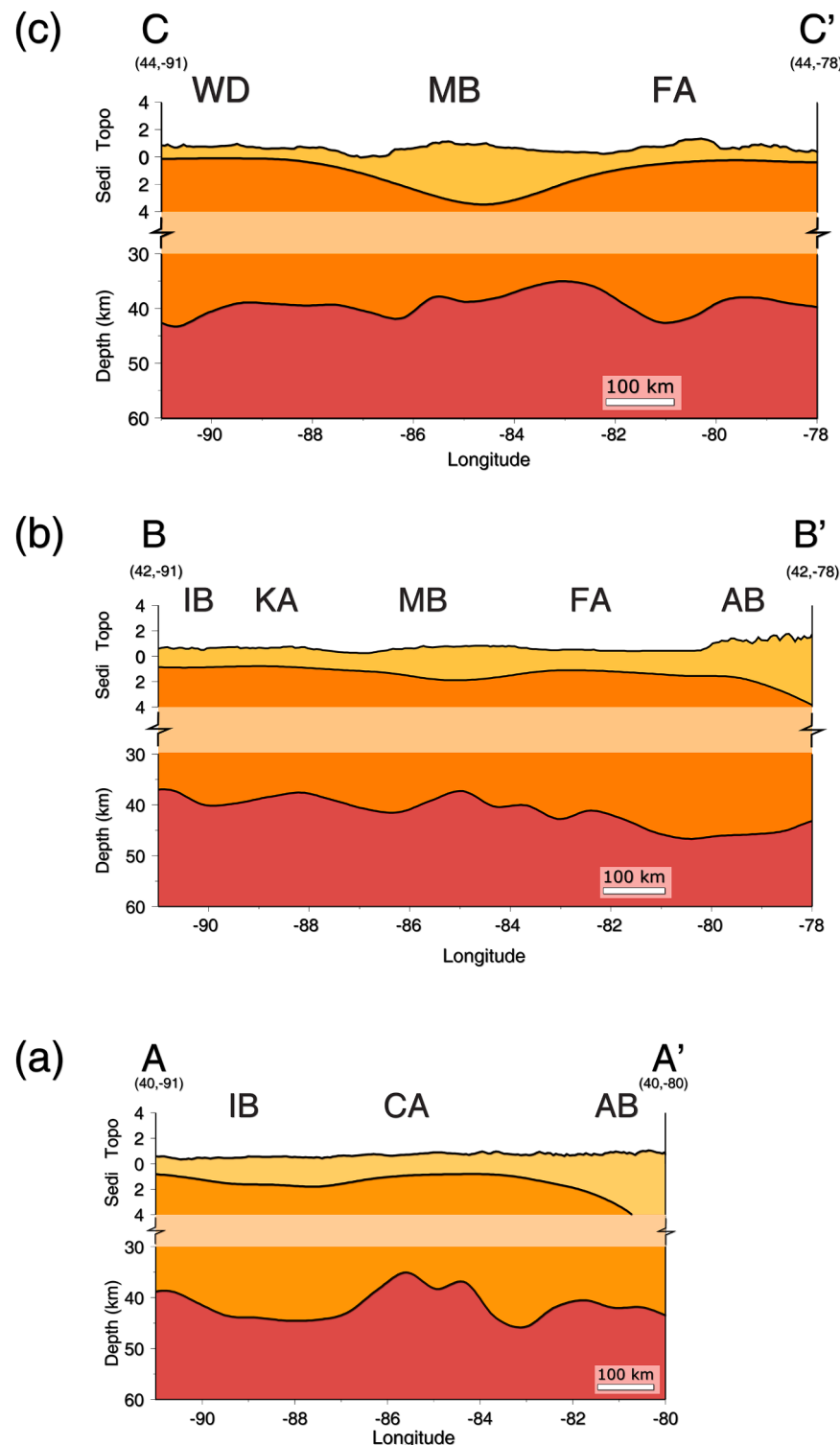


**Fig. 6.** Three vertically exaggerated cross sections showing crustal thickness variations based on the data provided in Fig. 5; the locations of the sections are provided on Fig. 5b. Each cross section shows land-surface topography (based on ETOPO1), the depth variations of the Great Unconformity (i.e., the thickness of cratonic-platform strata; based on CRUST1.0), and the Moho. So that the figures do not take up too much room, we deleted the interval between 30 and 4 km (represented by the light orange band). (a) Profile AA'. (b) Profile BB'; (c) Profile CC'. Topography, the Sediment Thickness (the Great Unconformity) and Moho of profile AA', BB', CC'. Abbreviations are the same as in Fig. 1a.

possibility that in some localities, lithospheric mantle velocities and lower crustal velocities are comparable; pinpointing Moho depth in such regions is difficult. Zhang et al. (2016) noted this challenge when they imaged the Moho underneath the western branch of the western arm of the Midcontinent rift using

traditional H-k stacking; their results show two possible boundaries, one at about 60 km and one at about 40 km. (Zhang et al. preferred the 60 km boundary, based on results of waveform modeling that assumed a particular value for the thickness of sediment in the rift.) In contrast, our results for the eastern arm of

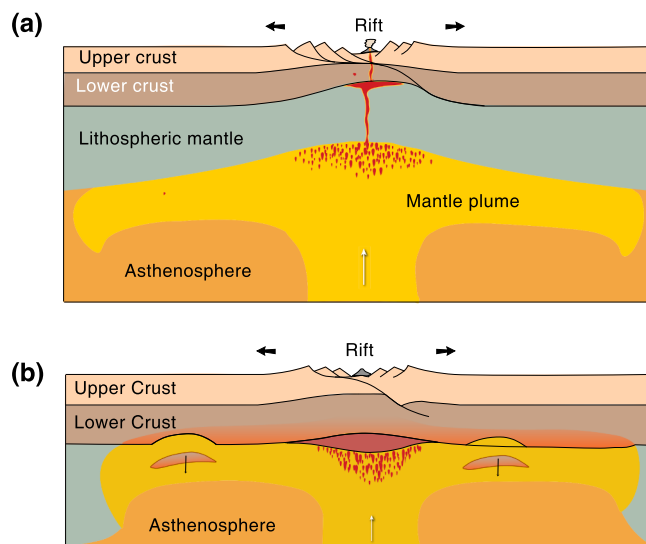


**Fig. 7.** Mechanisms for causing crustal thickness variations. (a) Differential underplating happens where lenses of mafic sills attach to the base of the crust. Not all of these are necessarily directly beneath a rift. (b) Differential delamination thins crust unevenly when dense eclogite can sink directly into the asthenosphere along with mantle plume heating.

the rift, place the Moho depth of this arm at about 40 km. Corrections incorporated in the H- $\kappa$ -c method did not indicate the possible existence of a lower boundary at 60 km.

### 5.3. Comparisons of Moho depth variations with gravity anomalies

Observed Bouguer gravity anomalies do not closely correspond to Moho depth within the Michigan Basin region (compare Fig. 8, based on Bonvalot et al., 2012, to Fig. 5). For example, two points (X and Y) along the midcontinent rift within the Michigan Basin region exhibit similar positive gravity anomaly values, whereas our Moho depth map indicates that the crust beneath Point X is 4 km thinner than the crust beneath point Y (Fig. 5). There are two possible explanations for the lack of correspondence.

First, isostasy was not fully achieved at both points. However, considering that both points share similar sediment thickness estimations (based on CRUST 1.0) and both share comparable tectonic histories (Whitmeyer and Karlstrom, 2007), this argument is less robust. In addition, the long-term stability of this crustal provinces suggests that contrasts in isostatic compensation would have had time to re-adjust. Second, the observed similar values in Bouguer gravity anomaly reflect differences in density profiles which balances gravity contrasts due to crustal thickness variations. The second possibility is more likely for, as noted by Yang et al. (2017), Xiao et al. (2022), underplating and/or delamination are two hypotheses that could significantly alter density profiles. Underplating introduces dense mafic material at the bottom of the crust, while delamination removes eclogitized lower crust, reducing average crustal density. In addition, variations in lithospheric mantle properties may contribute to the observed uncorrelated gravity anomalies (Cao et al., 2024). Further work is necessary to better understand the relationship between gravity anomalies and crustal thickness in cratonic platform areas.

## 6. Conclusions

Using the H- $\kappa$ -c method, we successfully compiled a higher-resolution Moho depth map (i.e., crustal-thickness variation map) of the northeastern portion of the cratonic platform in the United States, and the adjacent portion of the Canadian Shield. This region encompasses the several major epeirogenic structures. Our results show that

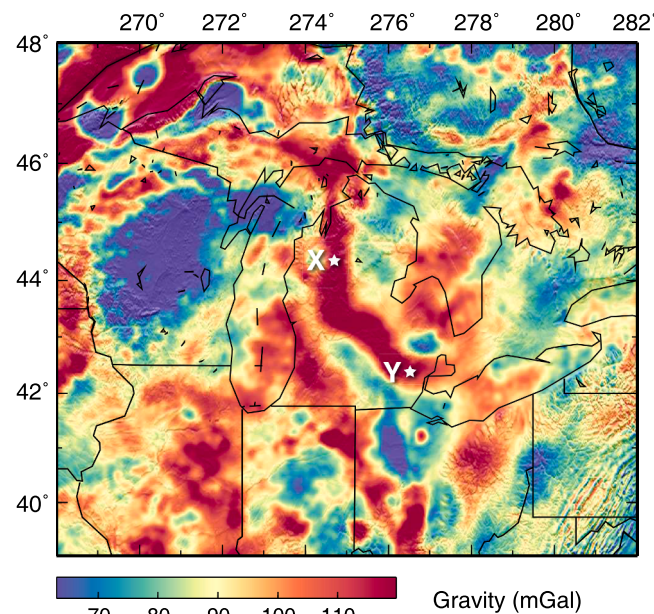


**Fig. 8.** Bouguer Gravity Anomaly of the Michigan Basin. White stars denote the locations of point X and point Y. This is constructed based on Bonvalot et al. (2012) (WGM 2012).

relief of the Moho is about 13 km, about third of the relief beneath the transition between the Indian Craton and the Himalayan orogen, but comparable to the relief across the East African Rift. Substantial Moho relief has also been observed across the Gulf of California (Persaud et al., 2007). Moho relief in our study area is twice the relief of the Great Unconformity, and about 18.6 times that of land surface topography. Notably, thinner crust underlies most domes and arches and thicker crust underlies most basins.

The undulation pattern of Moho depth found in the Illinois Basin (Xiao et al., 2022) persists beneath the Michigan Basin, but does not occur beneath the western Appalachian Basin. Though variations in Moho depth locally coincide with upper-crustal structures, such association does not stand out everywhere. In the northern part of our study area, we identified several north-south undulations, with wavelengths of about 150 km and amplitudes of about 7 km. These undulations do not coincide with the Yavapai-Mazatzal boundary, or with the trends of several rifts. They may reflect variations in crustal extension during Proterozoic rifting, differential underplating or delamination, or perhaps with Grenville-related crustal buckling. Notably, there is not a robust relationship in our study area between crustal thickness variations in the cratonic platform and Bouguer gravity anomalies. A comprehensive explanation of discordance between gravity anomalies and crustal thickness is not yet available.

## CRediT authorship contribution statement

**Hongyu Xiao:** Writing – review & editing, Writing – original draft, Visualization, Validation, Project administration, Methodology, Investigation, Formal analysis, Data curation, Conceptualization. **Stephen Marshak:** Writing – review & editing, Supervision, Conceptualization. **Michael DeLucia:** Writing – review & editing. **Xiaodong Song:** Writing – review & editing, Supervision, Funding acquisition, Conceptualization.

## Declaration of competing interest

The authors declare that they have no known competing financial interests or personal relationships that could have appeared to influence the work reported in this paper.

## Acknowledgments

We thank insightful and constructive comments from two anonymous reviewers, which helped in improving the manuscript. This research was supported by the China National Science and Technology Major Project (Grant 2024ZD1001101).

## Supplementary materials

Supplementary material associated with this article can be found, in the online version, at doi:10.1016/j.epsl.2025.119289.

## Data availability

Data will be made available on request.

## References

- Behrendt, J.C., Green, A.G., Lee, M.W., Hutchinson, D.R., Canon, W.F., Milkereit, B., Agena, W.F., Spencer, C., 1989. Crustal extension in the Midcontinent Rift system—Results from GLIMPCE deep seismic reflection profiles over Lakes Superior and Michigan. *Properties and Processes of Earth's Lower Crust*, 51, pp. 81–89.
- Bickford, M.E., Van Schmus, W.R., 1985. Discovery of two proterozoic granite-rhyolite terranes in the buried midcontinent basement: the case for shallow drill holes. *Observation of the Continental Crust through Drilling I: Proceedings of the International Symposium Held in Tarrytown, May 20–25, 1984*. Heidelberg: Springer Berlin Heidelberg, Berlin, pp. 355–364.
- Bonvalot, S., Balmino, G., Briais, A., Kuhn, M., Peyrefitte, A., Vales, N., Biancale, R., Gabalda, G. and Requin, F., 1989. “World gravity map: a set of global complete spherical Bouguer and isostatic anomaly maps and grids.” EGU general assembly conference abstracts. 2012.
- Cao, Z., Liu, L., 2024. Western US intraplate deformation controlled by the complex lithospheric structure. *Nat. Commun.* 15 (1), 3917.
- Chen, W.P., Jiang, Y., 2020. Undulating Moho beneath a near-uniform surface of central Tibet. *Earth Planet. Sci. Lett.* 543, 116343.
- Clerc, C., Ringenbach, J.C., Jolivet, L., Ballard, J.F., 2018. Rifted margins: ductile deformation, boudinage, continentward-dipping normal faults and the role of the weak lower crust. *Gondwana Res.* 53, 20–40.
- Cloetingh, S., Burow, E., 2011. Lithospheric folding and sedimentary basin evolution: a review and analysis of formation mechanisms. *Basin Res.* 23 (3), 257–290.
- Daniel, C.G., Indares, A., Medaris Jr, L.G., Aronoff, R., Malone, D. and Schwartz, J., 2023. Linking the Pinware, Baraboo, and Picuris orogens: recognition of a trans-Laurentian ca. 1520–1340 Ma orogenic belt.
- DeLucia, M.S., Guenther, W.R., Marshak, S., Thomson, S.N., Ault, A.K., 2018. Thermochronology links denudation of the Great Unconformity surface to the supercontinent cycle and snowball Earth. *Geology* 46 (2), 167–170.
- DeLucia, M.S., Murphy, B.S., Marshak, S., Egbert, G.D., 2019. The Missouri high-conductivity belt revealed by magnetotelluric imaging: evidence of a trans-lithospheric shear zone beneath the Ozark Plateau, Midcontinent USA? *Tectonophysics* 753, 111–123.
- Deng, Y., Li, J., Peng, T., Ma, Q., Song, X., Sun, X., Shen, Y., Fan, W., 2019. Lithospheric structure in the Cathaysia block (South China) and its implication for the Late mesozoic magmatism. *Phys. Earth Planet. Inter.* 291, 24–34.
- Gao, X., Li, Y., Yang, X., Ren, Z., 2022. Crustal structure beneath the central and western North China from receiver function analysis. *Earthq. Sci.* 35 (6), 448–473.
- Gordon, M.B., Hempton, M.R., 1986. Collision-induced rifting: the Grenville orogeny and the Keweenawan rift of North America. *Tectonophysics* 127 (1–2), 1–25.
- Hinze, W.J., Chandler, V.W., 2020. Reviewing the configuration and extent of the Midcontinent rift system. *Precambr. Res.* 342, 105688.
- Karlstrom, K.E., Humphreys, E.D., 1998. Persistent influence of proterozoic accretionary boundaries in the tectonic evolution of southwestern North America: interaction of cratonic grain and mantle modification events. *Rocky Mt. Geol.* 33 (2), 161–179.
- Kay, R.W., Kay, S.M., 1993. Delamination and delamination magmatism. *Tectonophysics* 219 (1–3), 177–189.
- Laske, G., Masters, G., Ma, Z., Pasyanos, M., 2013. Update on CRUST1. 0—A 1-degree global model of Earth's crust. *Geophys. Res. Abstr.* 15 (15), 2658.
- Leighton, M.W., 1996. Interior cratonic basins: a record of regional tectonic influences.
- Li, J., Song, X., 2021. Crustal structure beneath the Hi-CLIMB seismic array in the central-western Tibetan Plateau from the improved H-k-c method. *Earthq. Sci.* 34 (3), 199–210.
- Li, Z.X., Bogdanova, S., Collins, A.S., Davidson, A., De Waele, B., Ernst, R.E., Fitzsimons, I.C.W., Fuck, R.A., Gladkochub, D.P., Jacobs, J., Karlstrom, K.E., 2008. Assembly, configuration, and break-up history of Rodinia: a synthesis. *Precambr. Res.* 160 (1–2), 179–210.
- Li, J., Song, X., Wang, P., Zhu, L., 2019. A generalized H-k method with harmonic corrections on Ps and its crustal multiples in receiver functions. *J. Geophys. Res. Solid Earth* 124 (4), 3782–3801.
- Li, M., Song, X., Li, J., Bao, X., 2022. Crust and upper mantle structure of East Asia from ambient noise and earthquake surface wave tomography. *Earthq. Sci.* 35 (2), 71–92.
- Lister, G.S., Etheridge, M.A., Symonds, P.A., 1986. Detachment faulting and the evolution of passive continental margins. *Geology* 14 (3), 246–250.
- Liu, J., Zhang, J., Yin, C., Cheng, C., Liu, X., Zhao, C., Chen, Y., Wang, X., 2020. Synchronous A-type and adakitic granitic magmatism at ca. 2.2 Ga in the Jiao-Liao-Ji belt, North China Craton: implications for rifting triggered by lithospheric delamination. *Precambr. Res.* 342, 105629.
- Lustrino, M., 2005. How the delamination and detachment of lower crust can influence basaltic magmatism. *Earth Sci. Rev.* 72, 21–38.
- Marshak, S., Paulsen, T., 1996. Midcontinent US fault and fold zones: a legacy of proterozoic intracratonic extensional tectonism? *Geology* 24 (2), 151–154.
- Marshak, S., Paulsen, T., 1997. Structural style, regional distribution, and seismic implications of midcontinent fault-and-fold zones, United States. *Seismol. Res. Lett.* 68 (4), 511–520.
- Marshak, S., van der Pluijm, B.A., 2021. Tectonics of the continental interior in the United States. In: Alderton, D., Elias, S. (Eds.), *Encyclopedia of Geology*, 2nd ed. Academic Press, Oxford, UK, pp. 173–186. <https://doi.org/10.1016/B978-0-08-102908-4.00139-9>.
- Marshak, S., Domrois, S., Abert, C., Larson, T., Pavlis, G., Hamburger, M., Yang, X., Gilbert, H., Chen, C., 2017. The basement revealed: tectonic insight from a digital elevation model of the Great Unconformity, USA cratonic platform. *Geology* 45 (5), 391–394.
- McBride, J.H., Leetaru, H.E., Keach, R.W., McBride, E.I., 2016. Fine-scale structure of the Precambrian beneath the Illinois Basin. *Geosphere* 12 (2), 585–606.
- McGlannan, A.J., Gilbert, H., 2016. Crustal signatures of the tectonic development of the North American midcontinent. *Earth Planet. Sci. Lett.* 433, 339–349.
- Medaris Jr, L.G., Singer, B.S., Jicha, B.R., Malone, D.H., Schwartz, J.J., Stewart, E.K., Van Lankveld, A., Williams, M.L., Reiners, P.W., 2021. Early mesoproterozoic evolution of midcontinental Laurentia: defining the geon 14 baraboo orogeny. *Geosci. Front.* 12 (5), 101174.
- Meissner, R., Mooney, W., 1998. Weakness of the lower continental crust: a condition for delamination, uplift, and escape. *Tectonophysics* 296 (1–2), 47–60.
- Moehler, D.P., Bowersox, J.R., Hickman, J.B., 2018. Zircon U-Pb geochronology of two basement cores (Kentucky, USA): implications for late mesoproterozoic sedimentation and tectonics in the eastern Midcontinent. *J. Geol.* 126 (1), 25–39.
- Murphy, B.S., DeLucia, M.S., Marshak, S., Ravat, D., Bedrosian, P.A., 2024. Magnetotelluric insights into the formation and reactivation of trans-crustal shear zones in precambrian basement of the eastern US Midcontinent. *Geol. Soc. Am. Bull.* 136 (7–8), 2661–2675.
- Persaud, P., Pérez-Campos, X., Clayton, R.W., 2007. Crustal thickness variations in the margins of the Gulf of California from receiver functions. *Geophys. J. Int.* 170 (2), 687–699.
- Sadler, B., Pulliam, J., 2023. Modeling crustal structure in the Permian Basin by waveform-matching P receiver functions and autocorrelograms with particle swarm optimization. *J. Geophys. Res. Solid Earth* 128 (6), e2023JB026730.
- Shaw, C.A., Karlstrom, K.E., 1999. The Yavapai-mazatzal crustal boundary in the southern Rocky Mountains. *Rocky Mt. Geol.* 34 (1), 37–52.
- Shen, W., Ritzwoller, M.H., 2016. Crustal and uppermost mantle structure beneath the United States. *J. Geophys. Res. Solid Earth* 121 (6), 4306–4342.
- Sloss, L.L., 1988. Tectonic evolution of the craton in phanerozoic time. *The Geology of North America* 2: 25–51.
- Stein, C.A., Stein, S., Merino, M., Randy Keller, G., Flesch, L.M., Jurdy, D.M., 2014. Was the Midcontinent rift part of a successful seafloor-spreading episode? *Geophys. Res. Lett.* 41 (5), 1465–1470.
- Stein, S., Stein, C.A., Elling, R., Kley, J., Keller, G.R., Wysession, M., Rooney, T., Frederiksen, A., Moucha, R., 2018. Insights from North America's failed Midcontinent Rift into the evolution of continental rifts and passive continental margins. *Tectonophysics* 744, 403–421.
- Thybo, H., Artemieva, I.M., 2013. Moho and magmatic underplating in continental lithosphere. *Tectonophysics* 609, 605–619.
- Tikoff, B., Siddoway, C., Sokoutis, D., Willingshofer, E., 2022. The lithospheric folding model applied to the Bighorn uplift during the Laramide orogeny.
- Van Schmus, W.R., Schneider, D.A., Holm, D.K., Dodson, S., Nelson, B.K., 2007. New insights into the southern margin of the archean-Proterozoic boundary in the north-central United States based on U-Pb, Sm-Nd, and Ar-Ar geochronology. *Precambr. Res.* 157 (1–4), 80–105.
- Wang, Q., Song, X., Ren, J., 2017. Ambient noise surface wave tomography of marginal seas in East Asia. *Earth Planet. Phys.* 1 (1), 13–25.
- Wang, X., Zhan, Z., Zhong, M., Persaud, P., Clayton, R.W., 2021. Urban basin structure imaging based on dense arrays and bayesian array-based coherent receiver functions. *J. Geophys. Res. Solid Earth* 126 (9), e2021JB022279.
- Wessel, P., Smith, W.H., 1998. New, improved version of Generic Mapping Tools released. *Eos Trans. Am. Geophys. Union* 79 (47), 579–579.
- Whitmeyer, S.J., Karlstrom, K.E., 2007. Tectonic model for the proterozoic growth of North America. *Geosphere* 3 (4), 220–259.
- Xiao, H., DeLucia, M., Song, X., Li, J., Marshak, S., 2022. Crustal thickness variations in the Central Midcontinent, USA, and their tectonic implications: new constraints obtained using the H-k-c method. *Geophys. Res. Lett.* 49 (17), e2022GL099257.
- Yang, X., Pavlis, G.L., Hamburger, M.W., Marshak, S., Gilbert, H., Rupp, J., Larson, T.H., Chen, C., Carpenter, N.S., 2017. Detailed crustal thickness variations beneath the Illinois Basin area: implications for crustal evolution of the midcontinent. *J. Geophys. Res. Solid Earth* 122 (8), 6323–6345.
- Zandt, G., Gilbert, H., Owens, T.J., Dueca, M., Saleeby, J., Jones, C.H., 2004. Active foundering of a continental arc root beneath the southern Sierra Nevada in California. *Nature* 431 (7004), 41–46.
- Zhang, H., van der Lee, S., Wolin, E., Böllmann, T.A., Revenaugh, J., Wiens, D.A., Frederiksen, A.W., Derbyshire, F.A., Aleqabi, G.I., Wysession, M.E., Stein, S., 2016.

- Distinct crustal structure of the North American Midcontinent Rift from P wave receiver functions. *J. Geophys. Res. Solid Earth* 121 (11), 8136–8153.
- Zhang, B., Bao, X., Xu, Y., 2020. Distinct orogenic processes in the south-and north-central Tien Shan from receiver functions. *Geophys. Res. Lett.* 47 (6), e2019GL086941.
- Zhu, L., Kanamori, H., 2000. Moho depth variation in southern California from teleseismic receiver functions. *J. Geophys. Res. Solid Earth* 105 (B2), 2969–2980.